

Ripple-Induced Energetic Particle Loss in Tokamaks

R. B. White, R. J. Goldston, M. H. Redi, R. V. Budny

Plasma Physics Laboratory, Princeton University, P.O.Box 451,

Princeton, New Jersey 08543

Abstract

The threshold for stochastic transport of high energy trapped particles in a tokamak due to toroidal field ripple is calculated by explicit construction of primary resonances, and a numerical examination of the route to chaos. Critical field ripple amplitude is determined for loss. The expression is given in magnetic coordinates and makes no assumptions regarding shape or up-down symmetry. An algorithm is developed including the effects of prompt axisymmetric orbit loss, ripple trapping, convective banana flow, and stochastic ripple loss, which gives accurate ripple loss predictions for representative Tokamak Fusion Test Reactor and International Thermonuclear Experimental Reactor equilibria. The algorithm is extended to include the effects of collisions and drag, allowing rapid estimation of alpha particle loss in tokamaks.

PACS numbers: 52.55.Gb

I. Introduction

Loss of alpha particles or other high energy particles due to field ripple caused by the discrete toroidal field coils is an important consideration in the design of magnetic fusion devices. Collisionless losses are due to prompt axisymmetric orbit loss, ripple trapping, ripple-induced convective banana flow, and stochastic ripple loss. This work extends a previous calculation¹ due to Goldston, White, and Boozer (GWB), where stochastic threshold was estimated using phase decorrelation arguments, to explicitly calculate the resonance locations and widths, and explore the route to chaos. An expression for the stochastic threshold is found, and an algorithm is developed for energetic particle loss including the effects of prompt axisymmetric orbit loss, ripple trapping, convective banana flow, and stochastic ripple loss which gives reasonable accuracy in the estimation of collisionless loss in a tokamak. The calculation is carried out in general magnetic coordinates, giving expressions which can be directly applied to high pressure and noncircular equilibria without up-down symmetry, and the results are illustrated for alpha particle loss in the Tokamak Fusion Test Reactor² (TFTR) and the International Thermonuclear Experimental Reactor³ (ITER).

Any axisymmetric equilibrium field can be expressed in contravariant and covariant form through the equations^{4,5}

$$\vec{B}_0 = \vec{\nabla}\zeta \times \vec{\nabla}\Psi_p + q\vec{\nabla}\Psi_p \times \vec{\nabla}\theta, \quad (1)$$

$$\vec{B}_0 = g\vec{\nabla}\zeta + I\vec{\nabla}\theta + h\vec{\nabla}\Psi_p, \quad (2)$$

with Ψ_p the poloidal flux, θ the poloidal angle, and ζ a straight-field-line toroidal angle. The coordinate system is a straight field line one, i.e. $q(\Psi_p)$ (the safety factor) gives the local

helicity of a field line $q = d\zeta/d\theta$. The variable ζ is related to the geometric toroidal angle ϕ through $\zeta = \phi + \nu$, with ν a function of Ψ_p and θ , periodic in θ . The magnetic field strength $B_0(\Psi_p, \theta)$ is independent of the coordinate ζ .

The perturbation of the magnetic field strength due to the N toroidal field coils is represented by a modulation of the field amplitude

$$B(\Psi_p, \theta, \phi) = B_0(\Psi_p, \theta)(1 + \delta \cos(N\phi)), \quad (3)$$

with the ripple strength, δ , a function of position, determined by the coil geometry. The discrete coils also modulate the direction of the field, but the principal result for induced loss is due to the mirroring effect of the magnitude of B .

Particles trapped poloidally execute banana-shaped orbits, conserving energy E and magnetic moment μ with $E = mv_{\parallel}^2/2 + \mu B$. Guiding center motion in this field is given by a Hamiltonian formalism incorporated into the code ORBIT and described elsewhere⁵⁻⁷. In the following we use units given by the on-axis gyro frequency (time), and the major radius of the magnetic axis (distance). In these units $\rho = \sqrt{2E}$ is the gyro radius, which is the small parameter in the guiding center approximation.

Axisymmetry, or the absence of ripple, makes the toroidal canonical momentum $P_{\phi} = gv_{\parallel}/B - \Psi_p$ an integral of the motion, and this along with energy conservation means that all orbits are closed curves in the Ψ_p, θ plane. The banana tips describe constant Kolmogorov, Arnold, Moser (KAM) surfaces⁸ in the Ψ_p, ϕ plane. The KAM theory guarantees that for small ripple this phase space changes topologically only in a small region proportional to $\sqrt{\delta}$ where resonances produce islands. No diffusion can occur until these islands grow to overlap and produce chaotic wandering of orbits. To understand this process it is necessary

to investigate resonances in the banana tip motion.

In section II the route to chaos is investigated, and a reliable expression for stochastic threshold is found. The complications of up-down asymmetry and ripple wells are treated in section III. Section IV develops the algorithm for loss, and in section V comparisons of predicted loss with guiding center calculations are given. Section VI discusses collisions and drag, and the conclusions are summarized in section VII.

II. The Route to Chaos

Consider the discrete map generated by a trapped particle, each step of the map corresponding to the banana tip position (Ψ_p, ϕ) . As found in GWB the banana tip position is changed by the ripple, according to

$$d\Psi_p = \Delta_{\pm} \sin(N\phi \pm \pi/4), \quad (4)$$

where Δ_{\pm} , the displacement at the upper and lower banana tip, respectively, is due to the ripple and is given by an integral over the unperturbed trapped orbit, most of the contribution coming near the bounce point. The displacement amplitude is^{9-11,7}

$$\Delta_{\pm} = \frac{g\rho\delta T_{\pm}}{B(\partial_{\theta}B/B)^{1/2}}, \quad (5)$$

where

$$T_{\pm} = \frac{1}{2} \text{Re} \int_0^{\theta_b^{\pm}} d\theta \frac{e^{i3\pi/4} [e^{iNq(\theta - \theta_b^{\pm})} - 1]}{(\theta_b^{\pm} - \theta)^{3/2}} \simeq \sqrt{\pi Nq}, \quad (6)$$

and θ_b^{\pm} are the magnitudes of the upper and lower bounce angles, respectively. These expressions are the result of integrating the drift equations in general magnetic coordinates, so of course include the effects of equilibrium shape. The only essential approximation made

is that the dominant contribution of the ripple occurs near the banana tips, which permits Taylor expansions around θ_b^+ and θ_b^- . This leads to the simplified form of the integral T_{\pm} . The final expression for T_{\pm} has been checked numerically and gives reasonable accuracy even for small θ_b^{\pm} for typical values of N, q .

Each half bounce the particle moves $\pm q(\theta_b^+ + \theta_b^-)$ toroidally along the field, and in addition drifts across the field lines. The successive bounce points are given by the banana tip map, first found in GWB and studied by many authors¹²⁻¹⁹

$$\Psi_{p,t+1} = \Psi_{p,t} + \Delta_- \sin(N\phi_t) \quad (7)$$

$$N\phi_{t+1} = N\phi_t + N\phi_{b,t+1} + N\phi_{p,t+1} \quad (8)$$

$$\Psi_{p,t+2} = \Psi_{p,t+1} + \Delta_+ \sin(N\phi_{t+1}) \quad (9)$$

$$N\phi_{t+2} = N\phi_{t+1} - N\phi_{b,t+2} + N\phi_{p,t+2} \quad (10)$$

where $\phi_b = q(\theta_b^+ + \theta_b^-)$, and $\Psi_{p,t}$, ϕ_t is the initial position of the bounce point at the lower banana tip, and ϕ_p is the toroidal precession of the banana tip during one half bounce. The first equation describes the change of flux surface due to ripple at the lower bounce point, the second equation the toroidal motion between the lower and upper bounce points, etc. The total precession during one half bounce in the straight field line variable ζ is easily seen to be the same as precession in the toroidal variable ϕ , and is given⁷ by $\phi_p = \rho P(\Psi_p)$ with

$$P(\Psi_p) = \int_{-\theta_b^-}^{\theta_b^+} d\theta \left[\frac{g\rho_{\parallel}q'}{\rho} + \frac{\rho_{\parallel}(I' + qq')}{\rho} - \frac{(\mu + \rho_{\parallel}^2 B)(I + gq)\partial_{\Psi_p} B}{\rho\rho_{\parallel}B^2} \right], \quad (11)$$

a geometry-dependent integral independent of gyro radius, $\rho_{\parallel} = \sqrt{2E - 2\mu B}/B$; primes refer to derivatives with respect to Ψ_p .

Now we search the banana tip map for fixed points, which are the x- and o-points of resonances, for Δ_{\pm} arbitrarily small. Expressions in the banana tip map are given in terms of the unperturbed orbit. Ignoring corrections to Ψ_p of order Δ_{\pm}^2 and to ϕ of order Δ_{\pm} the total change in the position of the upper banana tip in one bounce is given by

$$d\Psi_p = \Delta_- \sin[N\phi] + \Delta_+ \sin[N(\phi + \phi_b + \phi_p)] \quad (12)$$

and

$$Nd\phi = 2N\phi_p \quad (13)$$

Period one fixed points (in the variable $N\phi$) are given by

$$2N\phi_p = 2k\pi \quad (14)$$

for all integers k. Similarly fixed points of period m are located approximately at $N\phi_p = k\pi/m$. Note that the flux surface location of the fixed points is entirely determined by the precession motion. Now search for resonances for fixed values of energy E and magnetic moment μ , a condition which makes the bounce angle in the unperturbed orbit a function of Ψ_p through $E = \mu B(\Psi_p, \theta_b)$. Consider first up-down symmetry. The toroidal location of the period one fixed points is then given by

$$2N\phi = 2l\pi - N(\phi_b + \phi_p) \quad (15)$$

for all integers l.

At each resonance surface $N\phi_p = k\pi$ the ripple produces islands in the motion of the banana tip with period one, with the two values of $N\phi$ in the interval $[0, 2\pi]$ giving the x-point and o-point locations. ‘‘Bounce resonances’’, with $N\phi_b = k\pi$, will be seen to play a

role only nonlinearly; the bounce motion produces no fixed points in the map at small ripple amplitude.

Now approximate ϕ_b and ϕ_p as linear functions in Ψ_p , a simplification certainly valid over the scale of the resonance spacing. Typically, for 3.5 Mev fusion alpha particles there are hundreds of precession and bounce resonances across the plasma. The resonance spacing in poloidal flux is then given approximately by

$$d\Psi_p = \frac{\pi}{N\phi'_p}. \quad (16)$$

For the purposes of analysis we replace the discrete points of the Poincaré map with continuous curves by introducing the differential time variable dt , with time measured in units of one half bounce. In the vicinity of a resonance surface the change in one bounce then takes the form

$$d\psi = 2\Delta \sin(N\phi + w) \cos(w) dt, \quad (17)$$

$$Nd\phi = 2N\phi'_p \psi dt, \quad (18)$$

where $\psi = \Psi_p - \Psi_{pk}$, $w = N\phi_b/2 + N\phi_p/2$, the \pm has been dropped in Δ since we are considering up-down symmetry, and the subscript k indicates evaluation at surface k. Dropping terms of order Δ^2 these equations can be integrated to yield

$$E(w, w_k) - E(w_k, w_k) = \pm \left[\frac{(1 + \phi'_b/\phi'_p)}{2} \right]^2 N\phi'_p \Delta [c_1 - \cos(N\phi + w_k)] \quad (19)$$

where

$$E(w, w_k) = \sum_{j=0}^{\infty} \frac{|E_{2j}| w^{2j+2}}{(2j+2)(2j)!} - w_k \ln \sqrt{\frac{1 + \sin w}{1 - \sin w}} \quad (20)$$

with E_n the Euler numbers. Since the original map is periodic in $N\phi_b$ and $N\phi_p$ we can take $-\pi/2 < w_k < \pi/2$. Integration constants have been chosen so that $c_1 = \pm 1$ describes the separatrix. The $k + 1$ st resonance surface is at $w = w_k + \pi(1 + \phi'_b/\phi'_p)/2$ or $N\phi'_p\psi = \pi$. In a typical equilibrium these derivatives vary significantly, so the properties of the map must be understood over a very large range. In TFTR, for example, again for 3.5 Mev alpha particles, $|\phi'_b/\phi'_p|$ typically has a mean of 10, a root mean square value of 30, and is greater than 50 in a very small part of the cross section. In ITER it typically has a mean of 80, and a root mean square value of 1000.

In Figs. 1, 2 are shown examples of the Poincaré map and the analytic representation given by Eq. 19 for $\Delta = 0.13$, $N\phi'_p = 1$, $N\phi'_b = 1$, $w_k = 0.6$. One period one precession resonance is shown and in Fig. 1 the period 2, 3, and 4 precession resonances are seen at $\psi \simeq -\pi/2$, $-\pi/3$, and $-\pi/4$ respectively. The value of w_k makes the map asymmetric and Eq. 19 is singular at $w = \pi/2$ or $\psi \simeq 1$.

For w_k very near $\pi/2$ the period-one island is split into two islands each of whose widths scale as Δ rather than $\sqrt{\Delta}$. The threshold is somewhat changed, but these islands in combination with islands from nearby regions still destroy surfaces. Note however that if $\phi'_b = \pm\phi'_p$, all islands vanish, and the map has good KAM surfaces for all Δ .

Stochastic threshold occurs in the manner described by Chirikov⁸, with the destruction of the last remaining KAM surface allowing diffusion of an orbit leading to loss. For $|\phi'_b/\phi'_p| \ll 1$ this occurs with increasing Δ , as precession islands of all periodicity grow until they overlap. In this case $|w - w_k| < 1$ can be used in $E(w, w_k)$ and we have approximately

$$(N\phi'_p\psi)^2 = \pm 2\cos(w_k)N\phi'_p\Delta[c_1 - \cos(N\phi + w)] \quad (21)$$

The Chirikov condition that neighboring primary islands overlap then gives an estimate for stochastic threshold

$$\Delta = \frac{\pi^2}{4N\phi'_p} \left[\frac{1}{\sqrt{|\cos(w_k)|} + \sqrt{|\cos(w_{k+1})|}} \right]^2 \quad (22)$$

with $w_{k+1} = w_k + \pi(1 + \phi'_b/\phi'_p)/2$, from which the infinity at $\phi'_b/\phi'_p = \pm 1$ and $w_k = \pi/2$ is apparent.

However, if $\phi'_b > \phi'_p$, as is usually the case, the results are very different, and the approach to stochastic threshold is dominated by the generation of nonlinear “bounce resonance” islands. For fixed Δ , increasing ϕ'_b leads to stochastic threshold, and yet the sizes of the period one precession islands *decrease* in this process because of the higher order terms in $E(w, a)$. Thus the sequence of precession islands cannot explain this approach to stochastic threshold. Instead, we observe nonlinear generation of additional islands caused by the bounce resonances, starting in the vicinity of the precession islands. Heuristically, the displacement caused by the precession resonances shifts ϕ_b across bounce resonances. This happens when ψ changes by the bounce resonance spacing $\pi/N\phi'_b$, and thus will be important only when the size of the precession island is comparable to it and the shift resonates with the bounce motion. Since the orbit modulation is strongest near the precession resonances the effect begins near them and expands from them as ϕ'_b or Δ increases. This is best observed for small Δ , so that precession islands are small and well separated. In Figs 3-7 are shown Poincaré maps of a period one island for fixed $\Delta = 0.01$, $N\phi'_p = 1$, with decreasing bounce resonance scale $s_b = \pi/(N\phi'_b)$. Observe first that the islands become rhomboid in shape (Fig. 3, $s_b = 0.16$) and then period doubling occurs by the creation of tall narrow islands at the original x-points (Fig. 4, $s_b = .1$) and the generation of small new satellite islands above

and below the initial one. The island width decreases in this process because of the higher order terms in $E(w, w_k)$. In Fig. 5 the island has shrunk almost to the bounce resonance scale and bounce resonance replication has occurred above and below it, and in Fig. 6 the scale s_b is comparable to island size. At this point the period doubled precession island has replicated to form five layers of islands. As ϕ'_b continues to increase this structure expands and approximates a web. In Fig. 7 is shown half the structure ($\psi > 0$) for $s_b = .04$, at which point it has expanded to $\psi = \pm 0.4$ with about 10 layers of replication. At the same time, higher period precession islands are being duplicated in similar fashions.

In Figs. 8-11 is shown the bounce resonance replication of a period three precession island chain, again for $\Delta = 0.01$, $N\phi'_p = 1$. Fig. 8 shows the initial chain at $\psi \simeq 2\pi/3$, $s_b = .08$. As ϕ'_b increases the islands grow (Fig. 9) and replicate (Fig. 10) once and twice (Fig. 11), at which point s_b is twice the island size. The relative importance of the different periodicities depends on the value of Δ . Only the period one islands have been observed to period double before replicating.

Of course for $\phi'_b < \phi'_p$ the threshold must revert to the Chirikov expression given by the precession resonances. An approximate expression for stochastic threshold was found in GWB,

$$\Delta_s = \frac{c}{N(|\phi'_p| + d|\phi'_b|)} \quad (23)$$

with $c = 1$ and $d = 1$. In Fig. 12 is shown the result of a numerical determination of threshold, averaged over a few values of w_k , by finding the minimum value of Δ allowing diffusion of at least one particle of a random set of 250 across one precession resonance spacing in 10^5 bounces. A better fit is obtained with $d = 0.5$, and $c = 1.0$, not far from the

small ϕ'_b Chirikov estimate, Eq. 22, with mean values of $\cos w_k$, $\cos w_{k+1} = 1/2$, $c = \pi^2/8$. One point at $\phi'_b/\phi'_p = 1000$ was also obtained using 10^7 bounces, and also fits this expression. A large number of bounces is needed to investigate stochastic threshold for large ϕ'_b/ϕ'_p since even well above threshold the diffusion is given by $(d\Psi_p)^2 = \Delta^2 t$ with t the time in units of the bounce period. Thus for very small Δ a very long run is necessary to ascertain whether there exists a KAM barrier to diffusion.

For small ϕ'_b/ϕ'_p , as is apparent from Eq. 22, there is some w_k dependence of Δ_s , and there even exist pathological cases; for example as noted before if $w_k = \pi/2$ and $\phi'_b = \pm\phi'_p$ there are no islands at all, and the map has good KAM surfaces everywhere for all values of Δ . Such cases do not of course occur in practice, where ϕ_b and ϕ_p are very different complicated functions of position, but the threshold can display significant local variations. In Fig. 13 is shown the result of a numerical determination of the threshold for small ϕ'_b/ϕ'_p and the full range of w_k . The isolated high threshold point at $w_k = \pi/2$ and $\phi'_b = \phi'_p$ is clearly seen. (The results have been truncated at 2 for plotting purposes; the narrow peak is infinite within computing limitations.) For $\phi'_b/\phi'_p > 4$ the rapid variation of the bounce motion within one precession resonance spacing smooths out the dependence on w_k and Eq. 23 is a good approximation. For up-down symmetry the results are independent of the sign of ϕ'_b . This is clearly seen from the map, since changing the sign of ϕ_b simply exchanges the upper and lower banana points (for a given value of w_k).

Control of shear in critical domains where the ripple is near threshold can modify the density of bounce resonances and perhaps change confinement. Lowering ϕ'_b is clearly beneficial, as seen in Eq. 23, but changes are not relevant unless the critical threshold for stochasticity can be made to exceed the local ripple value.

III. Asymmetry and Ripple Wells

Now consider the complications of up-down asymmetry and ripple wells. Note that both the precession resonance locations and the bounce motion involve both upper and lower bounce angles. Thus up-down asymmetry affects stochastic threshold primarily through the magnitudes of Δ_{\pm} . In Fig 14 is shown a threshold determination with unequal ripple values at the upper and lower bounce points. The numbers labeling the curves give the ratio of the smaller to the larger ripple value. For small asymmetry the threshold is modified only slightly from the value given by the larger ripple value, but when the ripple is zero at one bounce point the bounce motion no longer appears in the map, which reduces then to the Chirikov Taylor map with threshold $\Delta \simeq 1/(2N\phi'_p)$. An approximate fit, which matches this limiting value as well as Eq. 23, also shown in Fig. 14, is given by

$$\Delta_s = \frac{1}{N(|\phi'_p|(2 - r^p) + .5r^q|\phi'_b|)} \quad (24)$$

with r equal to the ratio of the smaller to the larger ripple value, p = 0.2, and q = 0.55, and Δ_s is the threshold value of the larger ripple amplitude. Asymmetry increases the threshold for large values of ϕ'_b/ϕ'_p .

In straight field line coordinates the condition for the existence of ripple wells is given simply by

$$|\partial_{\theta} B| < qBN\delta \quad (25)$$

If ripple wells occur at the location of alpha banana tips, new classes of collisionless loss mechanisms are possible, in addition to stochastic ripple diffusion. We consider the case with ripple wells on the side of the plasma in the direction of the grad-B drift direction, only on the opposite side of the plasma, and on both sides.

If ripple wells are located on the side of the plasma in the grad-B drift direction, then banana particles will trap collisionlessly in the ripple at their tips quite rapidly¹⁰. If the effective ripple increases along the drift trajectory (which is essentially a contour of constant $|B|$) - as is generally the case - the particles will exit from the plasma promptly.

If there are no ripple wells on the grad-B drift side of the plasma, but wells on the opposite side (due to up-down asymmetry), then toroidally localized trapping is not problematic, since the drift is radially inwards. However it was shown by Goldston and Jassby²⁰ that in this case banana-trapped particles drift outwards at a rate

$$v_r = \frac{v^2}{8\omega_c R} \left(\frac{\delta_*}{\epsilon}\right)^{1/2} \quad (26)$$

where δ_* represents the ‘effective’ well depth at the banana tip, as reduced by the axisymmetric variation of B along a field line, ϵ is the local inverse aspect ratio, and ω_c is the gyro frequency. As noted in that reference, this drift gives rise to very rapid loss of banana-trapped alpha particles. A specific calculation of the numerical coefficient for this drift velocity is provided by figure 12 of reference 10. However the radial drift is so rapid that the particles can be considered immediately lost, again so long as wells persist along the outward contour of $|B|$. It is interesting to note that vertical asymmetry causes no convective banana flow if local ripples are not present at either the top or bottom. This was shown numerically in reference 10, and analytically by one of us soon after. A more unified analysis along these same lines including an analytical derivation of the vanishing of the convective flow in the absence of ripple wells has since been published²¹.

In the case that ripple wells exist at both the top and bottom of the plasma, banana convection will only occur insofar as vertical asymmetry is present. However the presence

of the ripple wells on the grad-B drift side of the plasma will generally result in rapid loss even in the vertically symmetric case.

It is worth noting that our calculation of Δ (Eq. 5) assumes that inequality 25 is very far from being satisfied. Figure 13 of reference 10 suggests that the actual value of $\langle \Delta^2 \rangle$ can increase by a factor of up to 1.5 just at the boundary of the region with ripple-trapping.

IV. The Loss Algorithm

The threshold in the ripple amplitude for stochastic particle loss is

$$\delta_s = \frac{B\sqrt{\partial_\theta B/B}}{g\rho T}\Delta_s. \quad (27)$$

with Δ_s given by Eq. 24 for $|\phi'_b/\phi'_p| > 4$ and by the numerical results displayed in Fig. 13 for smaller values. Detailed comparison of these results to guiding center simulations with application to particular experiments involves an algorithm which takes into account ripple strength, geometry, and particle distribution. It is first necessary to evaluate threshold ripple values as a function of position, from Eq. 27. The loss domain is then constructed by forming the union of the stochastic domain, with $\delta > \delta_s$, the prompt loss domain, easily determined using conservation of energy and toroidal canonical momentum, and the ripple well domain. The resulting union must be then reduced by excluding all particles which, although in a loss domain, cannot leave the device without passing through a confinement region. This is easily determined since stochastic diffusion, banana convection and ripple well drift are along paths conserving the magnitude of B at the banana tip.

This loss domain for a given particle energy in the space of bounce tip location can be converted unambiguously to a domain in the space of magnetic moment and canonical

toroidal momentum μ , P_ϕ . Total loss for a given particle distribution is then found with standard Monte Carlo methods by ascertaining for each particle whether it is within the loss domain.

Although somewhat involved, this calculation of the loss for a distribution of 10^4 particles requires only seconds of computing time on the Cray Y-MP C90, whereas guiding center simulations require a fraction of an hour to determine collisionless loss and several hours to determine collisional loss with far fewer particles^{22,23}.

V. Stochastic Loss Calculations

A recent analysis^{22,23} of beam and alpha particle loss in TFTR using the simplest ripple threshold condition δ_{GWB} given by Eq. 3 in reference 1, not even the more complete Eq. 15 in that reference, required normalizations of this threshold value, the normalization being a factor of 7 smaller for loss of alphas than for 100 keV beam ions, clearly indicating the inadequacy of that simple criterion.

Some preliminary calculations have been made using the more complete algorithm described in Section IV for a number of equilibria with parameters of TFTR and ITER. These include a wide range of q-profiles, Shafranov shifts, magnetic axis locations, field strengths and particle energies. In Fig. 15 is plotted the stochastic loss predicted using the algorithm given in Section IV, and from guiding center Monte Carlo simulations, as a percent of the total distribution. Prompt losses, banana convection losses, and ripple well losses, also significant in some cases, but predicted analytically as well as observed with the guiding center code, have been subtracted out to better determine the accuracy of the stochastic ripple loss, by far the most difficult to estimate. By comparison the errors in the prompt, banana

convection, and ripple well losses are negligible. The comparison guiding center runs are collisionless at fixed energy, which require less time than do complete simulations including pitch angle scattering and slowing down. The runs were for about 8 msec of alpha particle lifetime, by which time the total loss had converged. The initial profiles were monoenergetic distributions of alpha particles ranging in energy from 100 keV to 3.5 MeV, with uniform pitch and a radial distribution of the form $(1 - r^2)^p$ in TFTR, with $p = 9, 5$, and 2 and r the midplane minor radius normalized to the plasma edge, and of the form $(1 - r)^3$ in ITER. Statistical errors in the guiding center loss runs resulting from \sqrt{n} with n the Monte Carlo loss number are shown with dashed lines. The statistical errors in the values given by the algorithm are small since 10^4 particles were used.

The TFTR and ITER equilibria were obtained with the PEST^{24,25} code through solution of the Grad-Shafranov equation using profile data obtained from TRANSP^{26,27}. In Fig. 16 is shown the 3.5 MeV alpha particle confinement domain for equilibrium 67885, a high current case with q on axis calculated to be 0.5 and $q=5.5$ at the plasma edge. All trapped particles with bounce tips outside the shaded regions suffer banana tip diffusion. Predicted collisionless stochastic loss is 3.4% . Numerical guiding center simulations give losses of $2.6 \pm 1\%$. The shape of this domain, very different from the almost circular domains given by the simplest GWB criterion, explains how the algorithm described in Section IV can be more successful than the simplest GWB estimate. The numerical values of Δ_s for small $|\phi'_b/\phi'_p|$ shown in Fig. 13 are significant in this determination. In Fig. 17 is shown the domain in which $|\phi'_b/\phi'_p| < 2$ for this equilibrium. Generally the use of the numerical values decreases the stochastic loss estimate, but the effect is not the same for all equilibria.

We also considered a reversed shear equilibrium with TFTR parameters, with $q=3$ on

axis, $q=2$ part way out, and $q=7$ at the plasma edge. For this equilibrium the algorithm predicts that all trapped alpha particles are lost either in one bounce orbit or stochastically. Predicted collisionless stochastic loss is 6.0%. Numerical guiding center simulations give losses of $5.5 \pm 1.5\%$.

We have also examined the new 20 coil ITER design, using equilibria and ripple values described in another publication²⁸. Losses for high current operation with $0.5 < q < 3.5$, both from the algorithm and from guiding center simulations, are below 0.1%. A reversed shear equilibrium in ITER has also been examined, with $q = 5$ on axis, 3.5 part-way out, and 6 at the 95% flux surface. The predicted stochastic loss is again negligible, but the asymmetry of the ripple gives large losses due to ripple well drift. In Fig. 18 is shown the extent of the ripple well domain for this reversed shear case. The asymmetry causes the ripple well domain to extend to the edge of the plasma in the upper half of the cross section, allowing loss directly to the wall. Collisionless losses predicted by the algorithm were 14%, and a guiding center simulation predicted 13.8% loss. This point is not included on Fig. 15. This loss rate could be problematic for such an operating mode in ITER.

In Fig 19 are shown the domains of axisymmetric confinement and prompt loss in the space of $\mu B_0/E$ with B_0 the on-axis toroidal field strength, and P_ϕ , normalized to the poloidal flux at the wall, for 3.5 Mev alpha particles in the TFTR equilibrium 67885. We show only the principal domain separations, there are in addition some small domains of non standard orbits. See Hsu and Sigmar²⁹ for a more complete description of this representation. The domain T-C consists of particles which are trapped and confined. Also shown are passing confined (P-C), passing loss (P-L), and trapped loss (T-L) domains. Domain A consists of passing particles which are lost for $v_{\parallel} > 0$ and confined for $v_{\parallel} < 0$. The slim leaf shaped

region labelled p consists of particles which do have a point on their trajectory at which the parallel velocity vanishes, but which nevertheless circle the magnetic axis (potato orbits). Note that at a banana tip $P_\phi = -\Psi_p$, so the two horizontal extremes of the trapped particle domain, $P_\phi/\Psi_w = -1$ and 0 correspond to banana tips at the outermost flux surface and at the magnetic axis respectively. Potato orbits are found near the magnetic axis at the intersection of the T-C and P-C domains. Stochastic loss involves only the T-C domain, which the presence of ripple splits into a confined part and a stochastic loss part.

The space of $\mu B_0/E$, P_ϕ can be used to provide significant diagnostic information regarding particle loss. In Fig 20 is shown the confined part of the T-C domain (shaded) including the effect of stochastic ripple loss, given by Eq. 27 for TFTR equilibrium 67885. The unshaded part of this domain (S-L) is predicted to be lost through stochastic ripple diffusion. The loss process conserves both E and μ so particles are lost by diffusing horizontally in this plot until they reach the prompt loss (T-L) boundary. Note that the potato orbits are well inside the confined domain. In Fig 21 are shown the *initial* particle positions of the confined particles in a guiding center simulation for the same equilibrium, with all particles initiated inside the T-C domain. In Fig. 22 are shown the *initial* positions for all particles which are lost in the guiding center simulation. The analytic domain in Fig. 20 slightly overestimates the loss (3.4% vs 2.6%). There are some confined particles shown in Fig. 21 which are in the loss domain of Fig. 20, and a few lost particles near the T-L boundary of Fig. 22 which are inside the confined domain of Fig. 20, but the algorithm predicts the loss fairly accurately. Also noticeable in Figs. 21,22 are some points outside the T-C boundary to the right. These are particles which do not circle the magnetic axis, but for which v_{\parallel} , although small, has no zero along the orbit, and they extend slightly beyond the boundary

of the diagram. Note that they are sufficiently affected by ripple that those adjacent to the stochastic loss domain are mostly lost. There are other subtleties of the representation, and we refer the reader to the article by Hsu and Sigmar for a complete discussion.

In Fig 23 are shown the *final* particle locations for the confined particles in a guiding center simulation for the TFTR reversed shear equilibrium, and in Fig. 24 are shown the *final* positions of the lost particles. Note that some of the lost particles have stepped rather far into the T-L domain. Since these particles are lost in one bounce orbit, this distance represents the step imparted by the ripple in a single bounce. The only particles not lost consist of a small fraction of the potato orbits, and some of the non-zero v_{\parallel} particles outside the upper boundary, whereas the algorithm predicts that all trapped particles are lost (6% vs 5.5%). Note from Fig. 23 that some of the non-zero v_{\parallel} particles outside the upper boundary are confined, but that those very close to the boundary are missing. Apparently those with v_{\parallel} closest to zero are stochastically lost by the ripple, but those with v_{\parallel} sufficiently far from zero are unaffected. These orbits are significantly different from those in equilibrium 67885 because of the larger q value near the origin. The analysis of the loss for these orbits will be the subject of a future study.

It has been suggested that potato orbits might have a low threshold for stochastic loss¹⁷ but these results indicate that their loss threshold might even be slightly higher than that given by the algorithm. In equilibrium 67885 they are all confined, and in the reversed shear equilibrium a small fraction of them are confined whereas the algorithm indicates they should be lost. Note that with ripple the boundaries of all domains are slightly modified, in that it is always slightly easier to strike the wall with ripple than in an axisymmetric equilibrium. Some of the lost particles in Fig. 24 are actually outside the T-L domain.

VI. Collisions and Drag

Pitch angle scattering is easily included in a guiding center code through the equation³⁰

$$\lambda' = \lambda(1 - \nu\tau) \pm [(1 - \lambda^2)\nu\tau]^{1/2} \quad (28)$$

with $\lambda = v_{\parallel}/v$ the pitch, τ the time step, and ν the collision frequency. This modification of the pitch can be performed each time step, and requires only that $\nu\tau \ll 1$. Collisional drag is given by a modification of the energy E ,

$$E' = E(1 - \nu_E\tau) \quad (29)$$

with ν_E the slowing down rate, similarly with the condition $\nu_E\tau \ll 1$. A related formalism using explicit Gaussian spreading in pitch and energy has been given previously²⁷.

The rates for pitch angle scattering and drag are very much slower than the basic guiding center time scale, the particle transit time. Thus it is numerically possible to artificially increase these rates significantly, speeding up the simulation²⁷. However, collisionless stochastic loss can take up to four or five hundred transit times to occur, and thus scattering and energy loss through drag cannot be artificially enhanced to the point that they would improperly interfere with the stochastic loss. Although the time for stochastic loss is very short compared to the slowing down time, it still represents significant computing time. Since the transit time is on the order of one microsecond, restricting the energy decrement to one percent in five hundred transit times completely precludes any enhancement, allowing no saving in computing time unless the stochastic loss process is also enhanced. This could be achieved by increasing the radial “kick” proportional to the square root of the collisional enhancement factor. Having a good algorithm for the stochastic loss domain is, however,

even simpler. It is then not necessary to wait for stochastic diffusion to occur; a particle can be counted as lost the moment it enters into this domain. In Fig. 25 is shown the confinement domain for 100 keV alpha particles for the same equilibrium as shown in Fig. 20. As the alpha particles thermalize, the confinement domain expands to cover the entire confined trapped particle region. Loss during slowing down is thus determined by the competition between the diffusion due to the pitch angle scattering, which can move particles into the loss domains, and the steady shrinking of these domains with decreasing energy. Typically in TFTR the alpha particle transit time is about 1μ sec, the bounce time about 10μ sec, slowing down time about 300 msec, and pitch angle scattering time about 25 sec at 3.5 MeV and 0.1 sec at 100 keV. The time step for ORBIT, with ripple, is about $\tau = 10^{-8}$ sec. Thus if stochastic particles are removed during the run it is possible to artificially increase the drag and pitch angle scattering by orders of magnitude, similarly decreasing the length of the run.

Similarly, increasing the pitch angle scattering can interfere with the effect of ripple trapping. Inclusion of the ripple trapping domain as part of the loss domain, i.e. counting particles as lost as soon as they enter the ripple well domain, treats the ripple well loss correctly while allowing an artificial increase of the pitch angle scattering rate.

The only disadvantage of this scheme is that one does not obtain a correct lost particle wall distribution, since the correct wall impact point is not obtained for those particles removed because they are in the stochastic or ripple well domains.

Full slowing down simulations of a number of cases reported previously²², and the reversed shear case, have been repeated with an artificial increase in the collision and drag coefficients by a factor of up to 500 and periodic ejection of particles found in the loss do-

main. Particle ejection was done at intervals ranging from 1/10th to 1/100th of the slowing down time, with no change in results. The computing time involved for a 1000 particle simulation was only 400 sec of CPU time compared to several hours for an unaccelerated simulation with 256 particles. Table 1 gives the results for these simulations. Some of the normal or unaccelerated simulations were carried out with more than 256 particles, the error for the particle loss in each case indicates the statistical deviation, obtained by dividing the particles of each run into ten groups and finding the standard deviation of the losses among them.

| Table 1. Collisional Simulations | | | | | | |
|----------------------------------|---------------|------|------------|---------|-------------|--------|
| Parameters | | | | | Loss % | |
| Device | Equilibrium | B kG | q profile | Axis cm | Accelerated | Normal |
| TFTR | 67885 | 48 | 0.96 - 6.2 | 280 | 18 ± 2 | 23 ± 4 |
| TFTR | 67241 | 45 | 0.83 - 15 | 293 | 37 ± 2 | 38 ± 4 |
| TFTR | 55851 | 45 | 1.0 - 5.6 | 266 | 19 ± 4 | 21 ± 4 |
| TFTR | R-S | 46 | 3.60 - 6.9 | 288 | 38 ± 2 | 33 ± 4 |
| ITER | 1001 | 57 | 0.54 - 3.5 | 839 | 0 ± 1 | 0 ± 2 |
| ITER | 1002 | 57 | 0.54 - 3.5 | 848 | 0 ± 1 | 0 ± 2 |
| ITER | post sawtooth | 57 | 0.54 - 3.5 | 848 | 9 ± 1 | 8 ± 2 |

The equilibrium ITER 1001 is an H-mode case, with a ramp density profile, and equilibrium 1002 is an L-mode case with density of the form $(1-r)^3$. The post sawtooth equilibrium is an L-mode case with a constant density profile for the poloidal flux less than 0.7 times the wall value. TFTR R-S is the reversed shear equilibrium discussed in Section V. These

results are sufficiently good to encourage the incorporation of the algorithm into routine data analysis and integrated systems design codes. Additional numerical experiments will be reported in future publications.

VII. Conclusion

An improved understanding of the approach to chaos leading to stochastic loss makes it possible to make reliable, rapid, collisionless alpha particle confinement predictions, which can be exercised in a wide range of plasma scenarios, as needed. This obviates the necessity for extensive time-consuming guiding center calculations. The loss algorithm includes the effects of prompt loss, ripple well trapping, banana convection, and stochastic ripple diffusion. An implementation of the loss algorithm into an artificially speeded up guiding center calculation makes possible complete guiding center loss estimates including drag and pitch angle scattering for full alpha particle slowing down times, in computing times short enough to allow incorporation of the algorithm into routine data analysis and integrated systems design codes.

ACKNOWLEDGMENTS

The authors are grateful to Mark Hermann and Bill Nevins for useful discussions, and to Janardhan Manickam and Don Monticello for assistance with equilibria. This work was supported by the U.S. Department of Energy under contract number DE-AC02-76-CHO3073.

REFERENCES

1. R. J. Goldston, R. B. White, and A. H. Boozer, *Phys. Rev. Lett.* **47**, 647 (1981).
2. R. Hawryluk, *Plasma Phys. Controlled Fusion* **33**, 1509 (1991).
3. K. Tomabechi, *Proceedings of the Twelfth International Conference on Plasma Physics and Controlled Nuclear Fusion Research*, International Atomic Energy Agency, Vienna, 1989 **3**, 214 (1989).
4. A. H. Boozer, *Phys. Fluids* **24**, 1999 (1981).
5. R. B. White and M. S. Chance, *Phys. Fluids* **27**, 2455 (1984).
6. R. B. White, *Phys. Fluids B* **2**, 845 (1990).
7. R. B. White, *Theory of Tokamak Plasma*, North Holland, 1989.
8. B. V. Chirikov, *Phys. Rep.* **52**, 263 (1979).
9. A. H. Boozer, *Phys. Fluids* **23**, 2283 (1980).
10. R. J. Goldston and H. H. Towner, *J. Plasma Phys.* **26**, 283 (1981).
11. P. N. Yushmanov, *Nucl. Fusion* **23**, 1599 (1983).
12. R. B. White, A. A. Boozer, R. Goldston, R. Hay, J. Albert, and C. F. F. Karney, *Plasma Phys. Controlled Nucl. Research* **3**, 391 (1983).
13. Y. I. Kolesnichenko and V. A. Yavorsky, *Proceedings of the Sixteenth European Conference on Controlled Fusion and Plasma Physics Research*, European Physical Society, 1989 **13**, 415 (1989).

14. V. Y. Goloborodko and V. A. Yavorsky, Proceedings of the Sixteenth European Conference on Controlled Fusion and Plasma Physics Research, European Physical Society, 1989 **13**, 419 (1989).
15. F. Zajtsev, A. P. Smirnov, and P. Yushmanov, Nucl. Fusion **26**, 1311 (1986).
16. Y. I. Kolesnichenko and V. A. Yavorsky, Nucl. Fusion **29**, 1319 (1989).
17. L. G. Eriksson and P. Helander, Nucl. Fusion **33**, 767 (1993).
18. P. G. J. P. Roubin, Nucl. Fusion **30**, 1499 (1990).
19. P. N. Yushmanov, Reviews of Plasma Physics **16**, 55 (1990).
20. R. J. Goldston and D. L. Jassby, Proceedings of Third International Meeting on Theoretical and Experimental Aspects of Heating of Toroidal Plasmas, Grenoble, Commissariat a l'Energie Atomique, Paris, Commission des Communautés Europeennes, Brussels **1**, 1 (1976).
21. P. N. Yushmanov, J. R. Cary, and S. G. Shasharina, Nucl. Fusion **33**, 1293 (1993).
22. M. H. Redi, M. C. Zarnstorff, R. B. White, R. V. Budny, A. C. Janos, D. K. Owens, J. F. Schivell, S. D. Scott, and S. J. Zweben, Nucl. Fusion **35**, 1191 (1995).
23. M. H. Redi, R. V. Budny, D. S. Darrow, H. H. Duong, R. K. Fisher, A. C. Janos, J. M. McChesney, D. C. McCune, S. S. Medley, M. P. Petrov, J. F. Schivell, S. D. Scott, R. B. White, M. C. Zarnstorff, and S. J. Zweben, Nucl. Fusion **35**, 1509 (1995).
24. R. C. Grimm, J. Greene, and J. L. Johnson, Methods Computing Physics **9**, 253 (1974).
25. R. C. Grimm, R. L. Dewar, and J. Manickam, J. Comput. Phys. **49**, 94 (1983).

26. R. Hawryluk, *Physics of Plasmas Close to Thermonuclear Conditions* **1**, 19 (1980).
27. R. Goldston, D. McCune, H. Towner, S. Davis, R. Hawryluk, and G. Schmidt, *J. Comput. Phys.* **43**, 61 (1981).
28. M. H. Redi, R. V. Budny, D. C. McCune, C. O. Miller, and R. B. White, *Phys. Plasmas* (1996).
29. C. T. Hsu and D. J. Sigmar, *Phys. Fluids* **4**, 1492 (1992).
30. A. H. Boozer and G. Kuo-Petravic, *Phys. Fluids* **24**, 851 (1981).

FIGURES

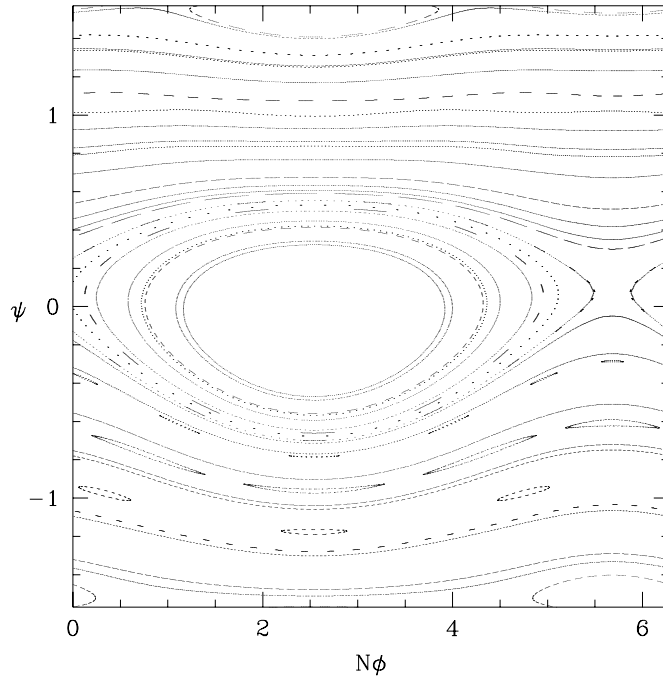


Fig. 1. Poincaré plot of precession island, $\Delta = 0.13$, $N\phi'_p = 1$, $N\phi'_b = 1$, $w_k = 0.6$.

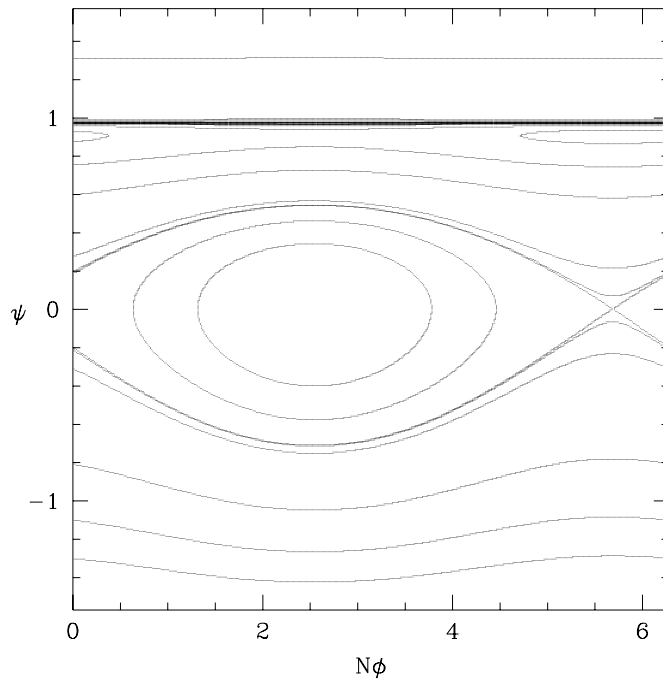


Fig. 2. Analytic representation of precession island from Eq. 19.

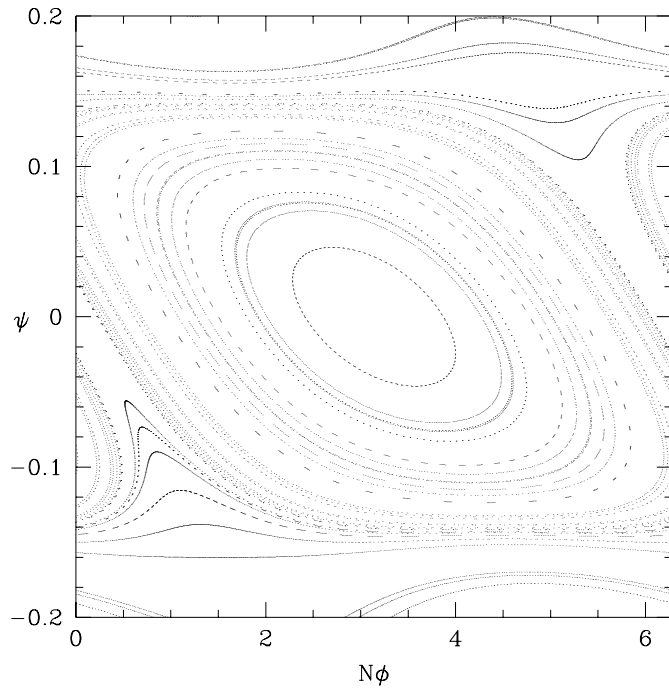


Fig. 3. Poincaré plot, $\Delta = 0.01$, $N\phi'_p = 1$, $s_b = 0.16$.

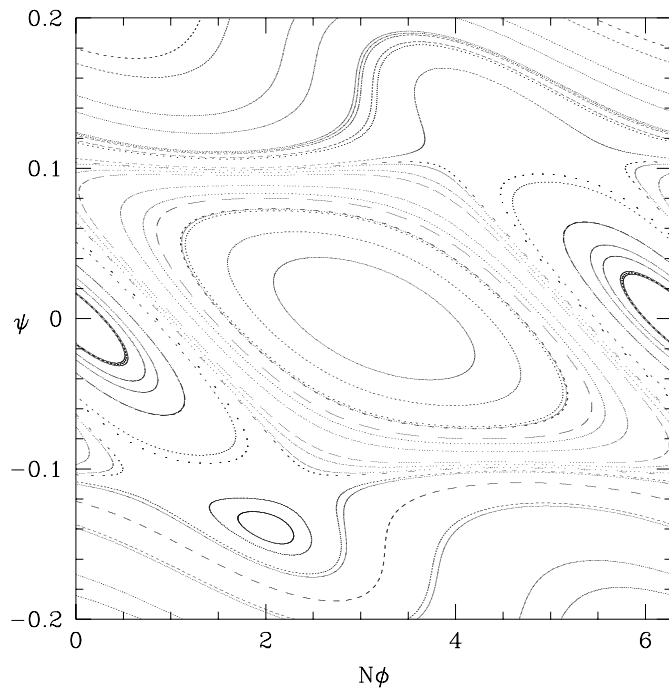


Fig. 4. Poincaré plot, $\Delta = 0.01$, $N\phi'_p = 1$, $s_b = 0.1$.

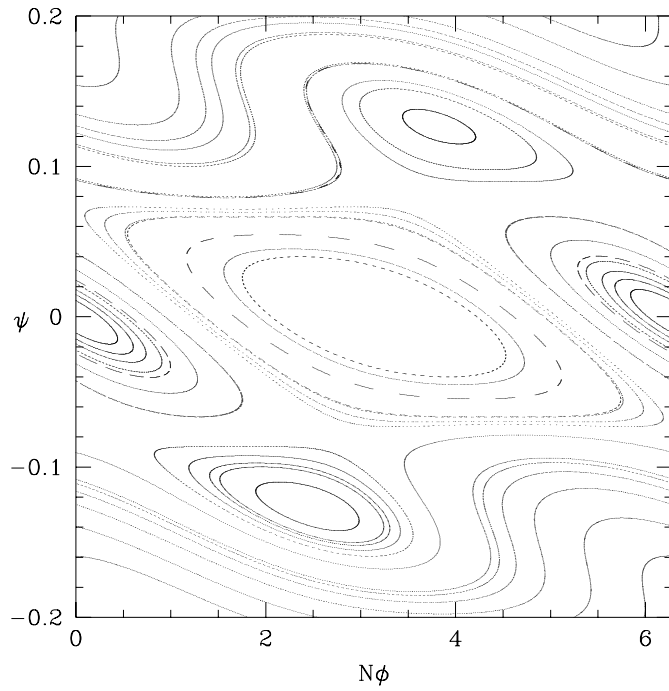


Fig. 5. Poincaré plot, $\Delta = 0.01$, $N\phi'_p = 1$, $s_b = 0.08$.

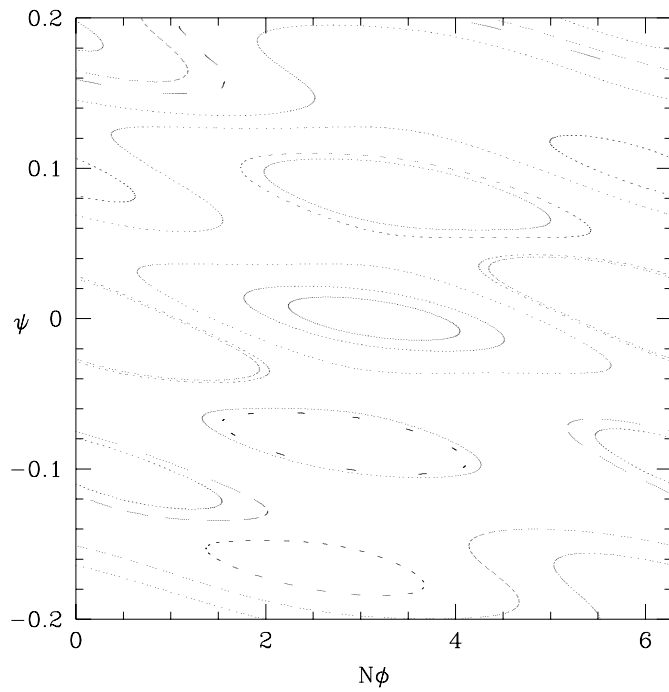


Fig. 6. Poincaré plot, $\Delta = 0.01$, $N\phi'_p = 1$, $s_b = 0.05$.

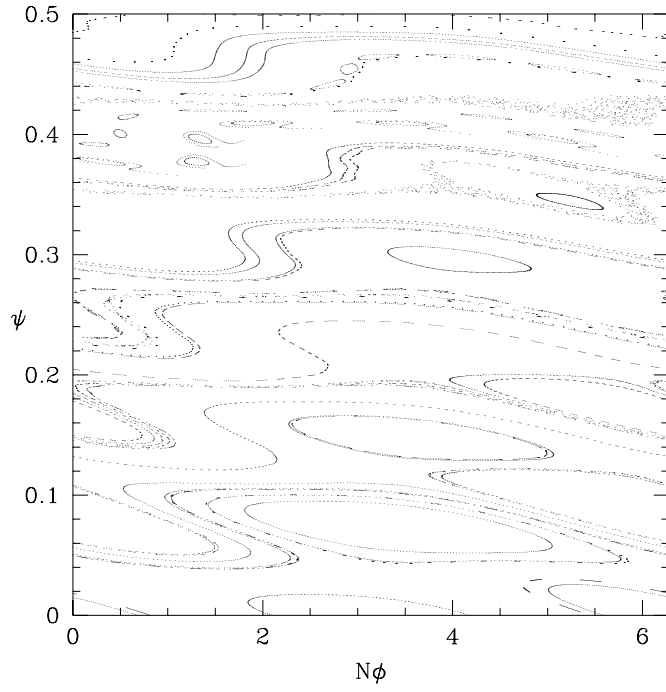


Fig. 7. Poincaré plot, $\Delta = 0.01$, $N\phi'_p = 1$, $s_b = 0.04$.

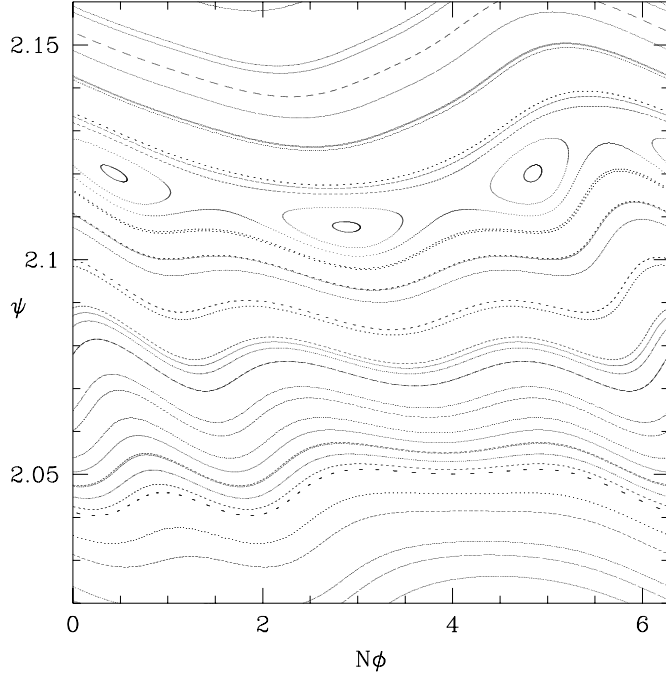


Fig. 8. Poincaré plot, $\Delta = 0.01$, $N\phi'_p = 1$, $s_b = 0.08$.

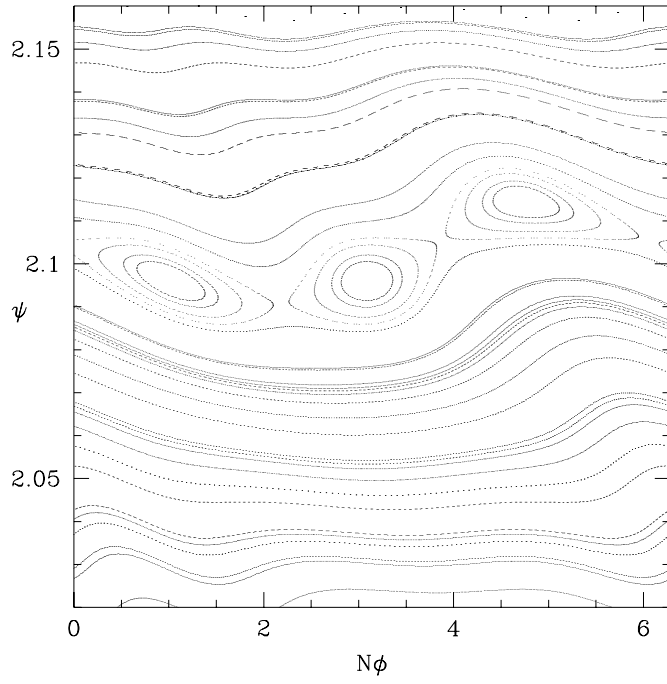


Fig. 9. Poincaré plot, $\Delta = 0.01$, $N\phi'_p = 1$, $s_b = 0.06$.

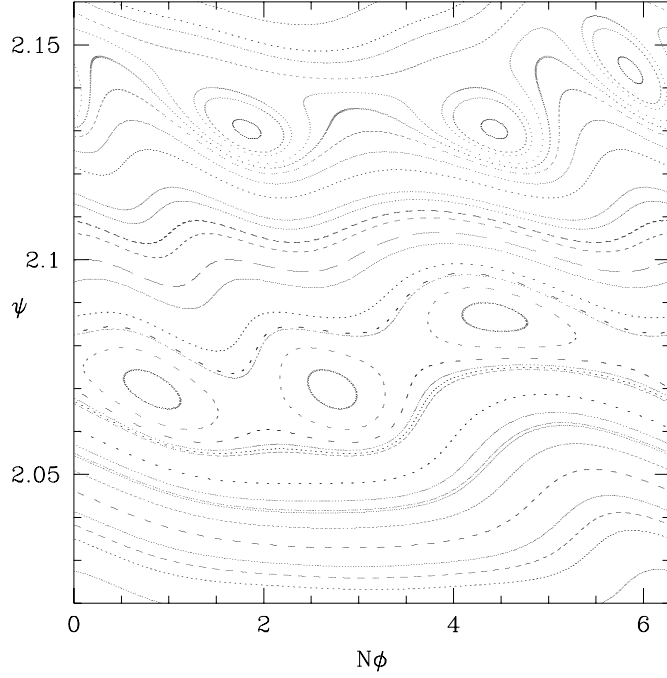


Fig. 10. Poincaré plot, $\Delta = 0.01$, $N\phi'_p = 1$, $s_b = 0.05$.

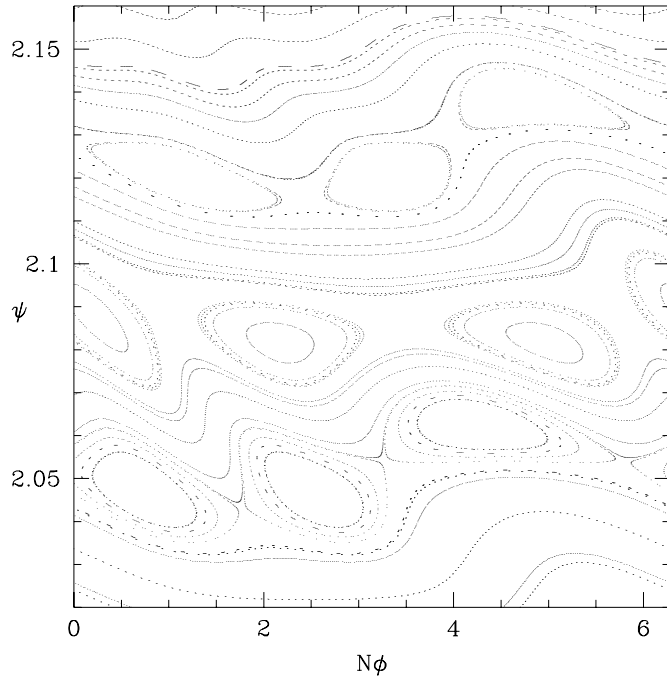


Fig. 11. Poincaré plot, $\Delta = 0.01$, $N\phi'_p = 1$, $s_b = 0.04$.

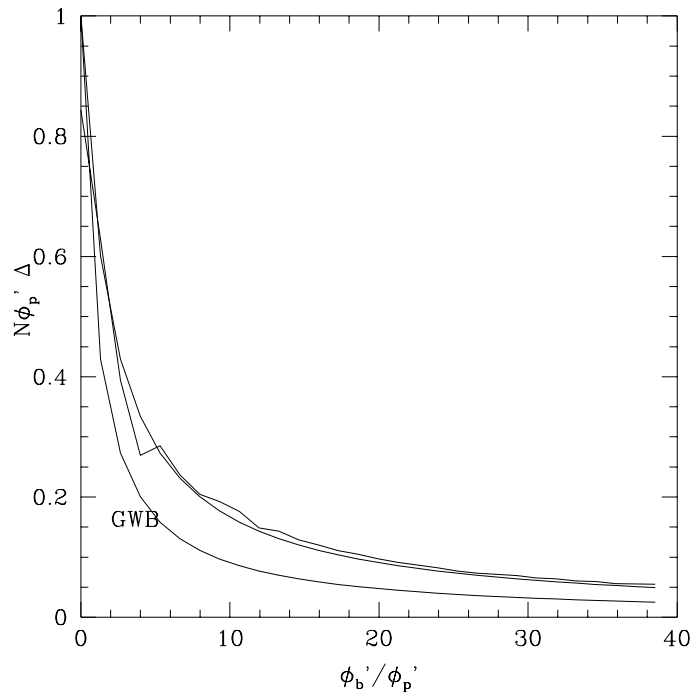


Fig. 12. Stochastic threshold (jagged line), Eq. 23, and the GWB estimate.

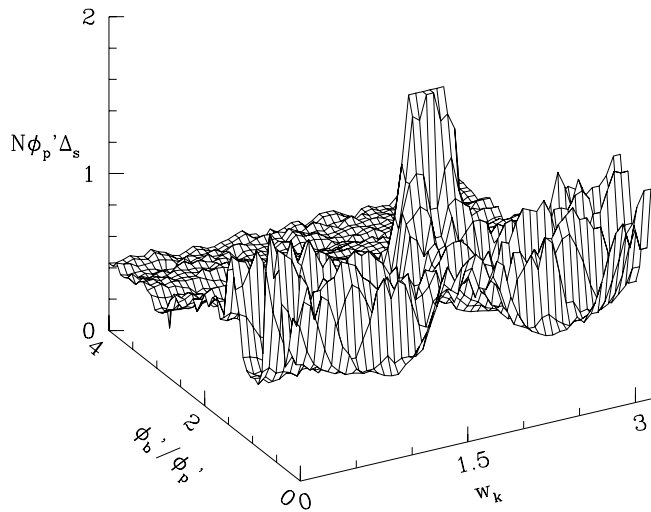


Fig. 13. Stochastic threshold for small ϕ_b' / ϕ_p'

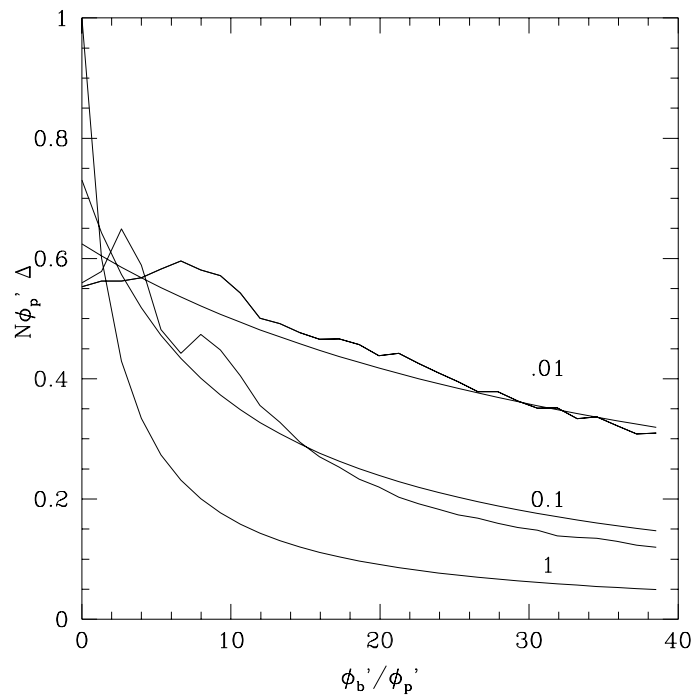


Fig. 14. Stochastic threshold for up-down asymmetry.

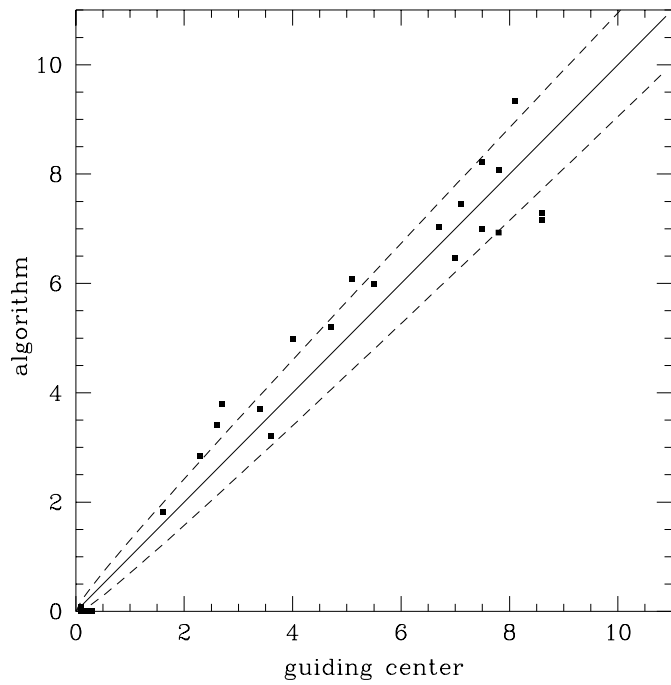


Fig. 15. Loss (%) , from Eq. 27 and by guiding center simulation.

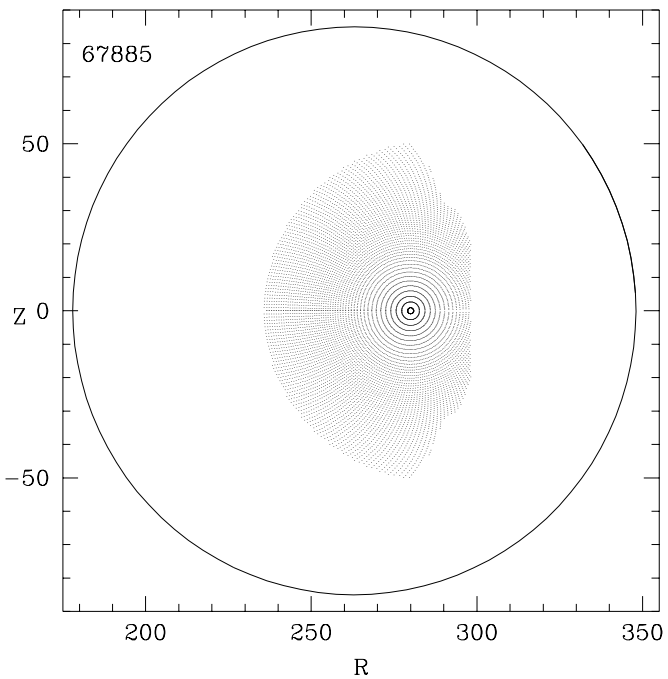


Fig. 16. Confinement domain in TFTR, equilibrium 67885.

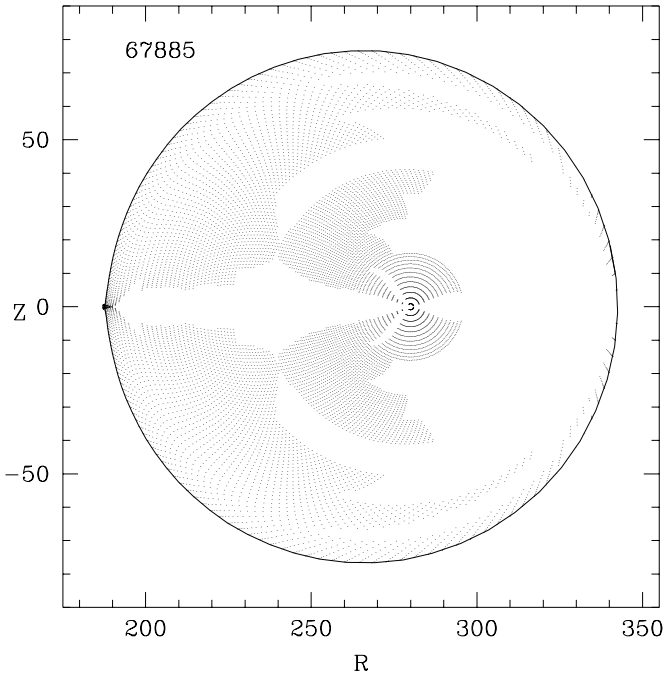


Fig. 17. Region with $|\phi'_b/\phi'_p| < 2$, equilibrium 67885.

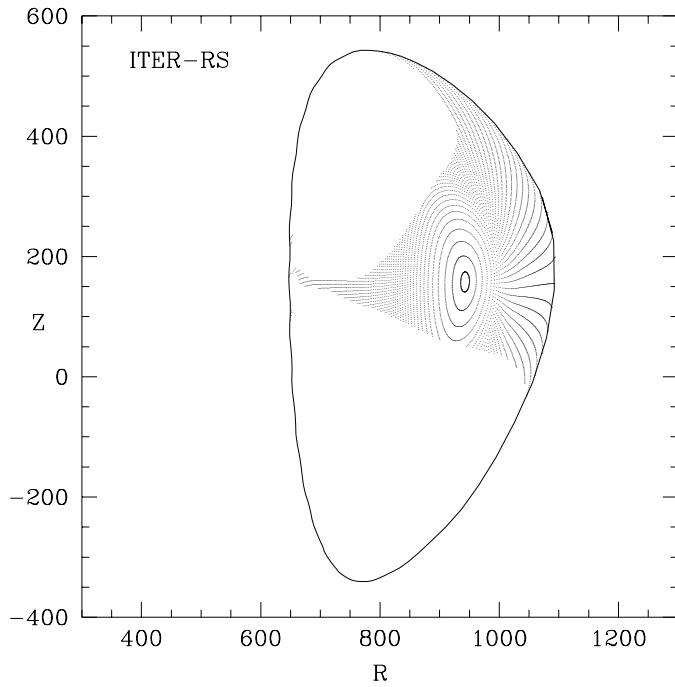


Fig. 18. Ripple well domain in ITER, reversed shear.

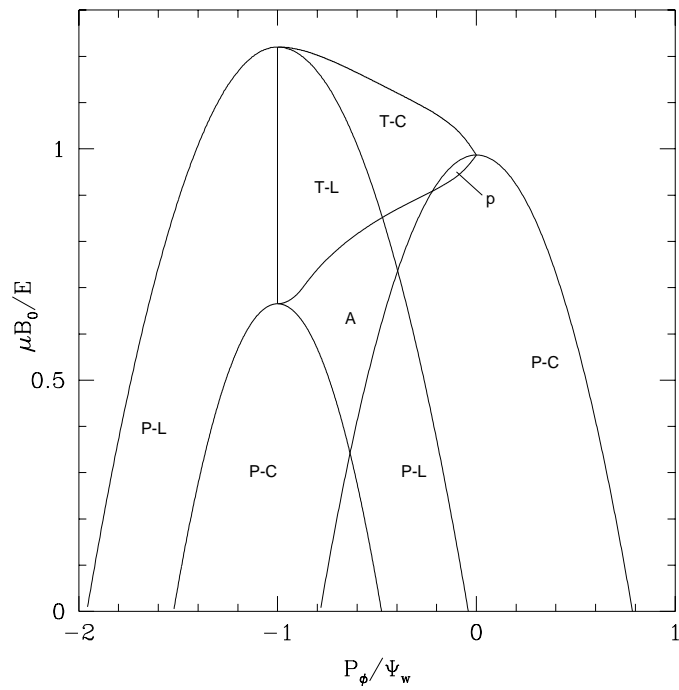


Fig. 19. Confinement domains in $\mu/E, P_\phi$.

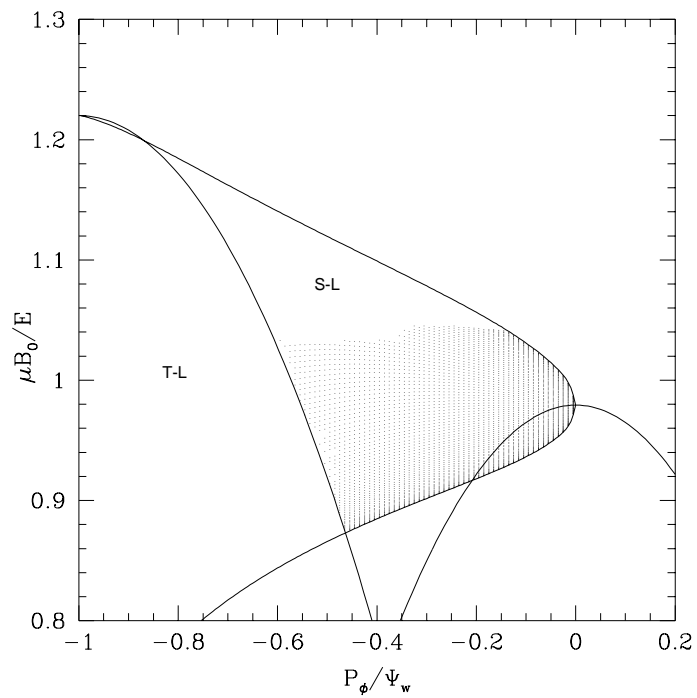


Fig. 20. Confinement domain, equilibrium 67885.

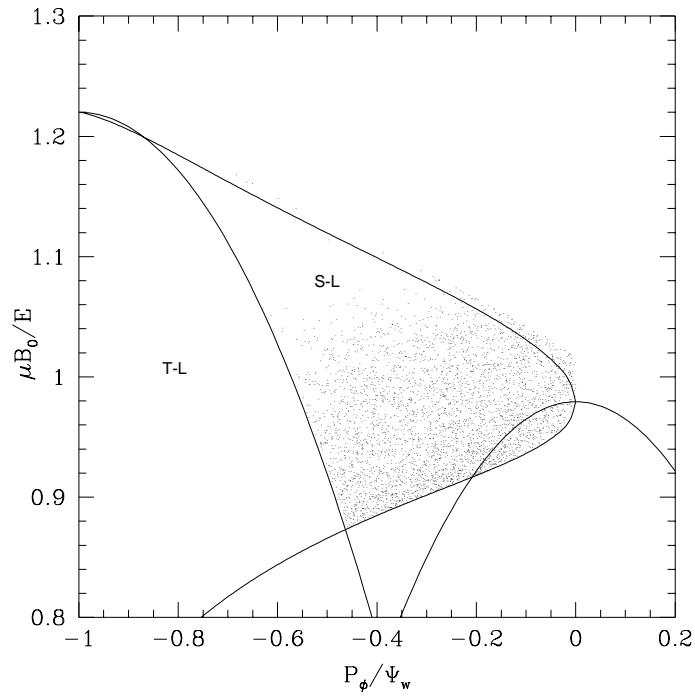


Fig. 21. Guiding center confinement domain, equilibrium 67885.

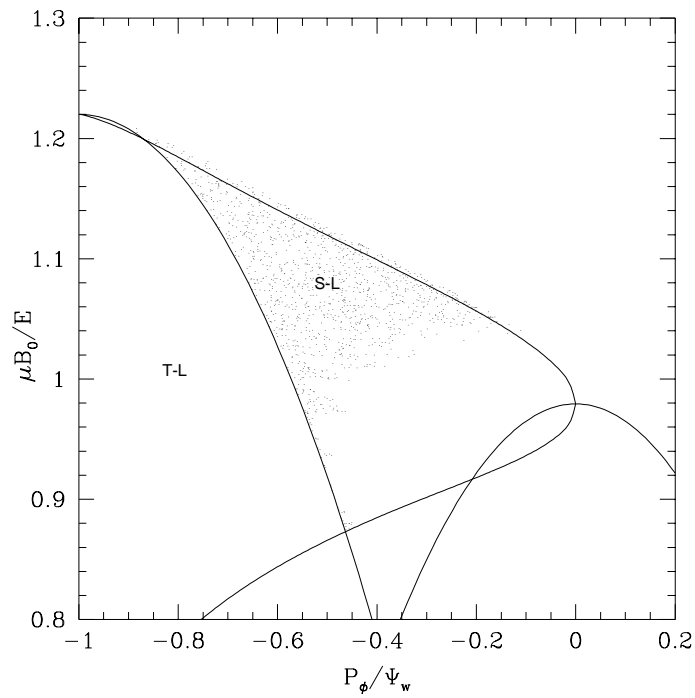


Fig. 22. Guiding center loss domain, equilibrium 67885.

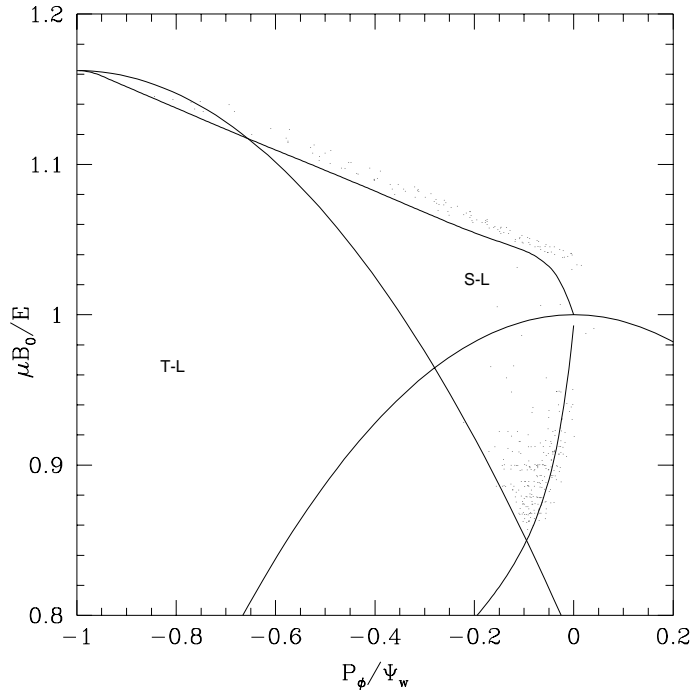


Fig. 23. Final positions of confined particles, R-S equilibrium.

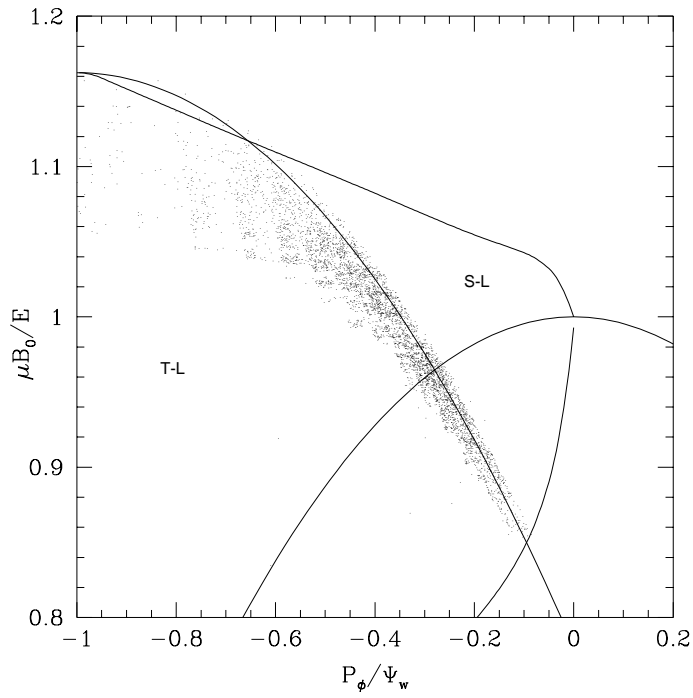


Fig. 24. Final positions of lost particles, R-S equilibrium.

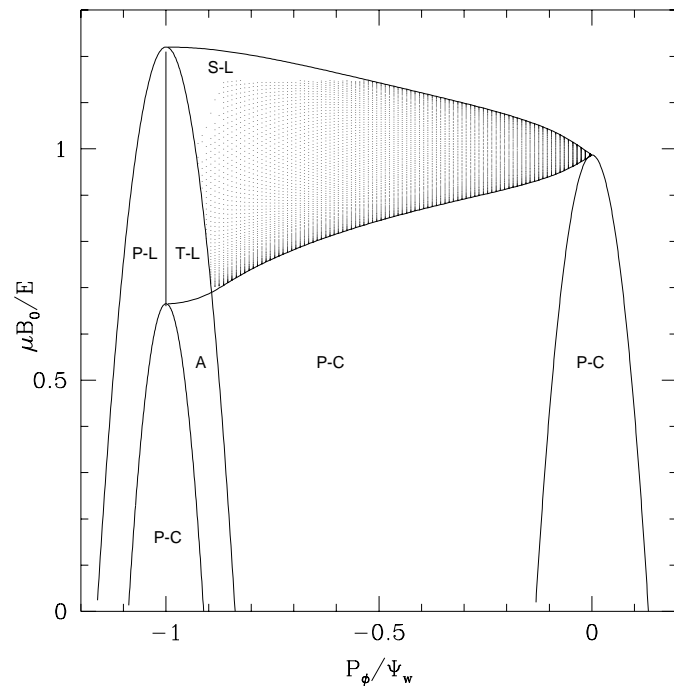


Fig. 25. Confinement domain, 100 keV, equilibrium 67885.